Applied and Computational Mechanics 20 (2026) XXX–YYY

$\mathcal{H}_\infty$ robust control for gust load alleviation of geometrically nonlinear flexible aircraft

N. D. Tantaroudas[a,*], I. Karachalios[b]

[a] Institute of Communications and Computer Systems (ICCS), Athens, Greece
[b] Department of Environment, School of Technology, University of Thessaly, Larissa, Greece

Received 2 April 2026; accepted 16 July 2026

Abstract

This paper presents an $\mathcal{H}_\infty$ robust control synthesis framework for gust load alleviation of very flexible aircraft exhibiting geometrically nonlinear structural behaviour. The controller is synthesised on a compact reduced-order model (ROM) comprising eight degrees of freedom for the unmanned aerial vehicle (UAV) configuration and nine for the flying-wing, obtained through nonlinear model order reduction of the coupled fluid-structure-flight dynamics system, and subsequently validated against the full nonlinear model (540 and 1 616 degrees of freedom, respectively). The control architecture utilises trailing-edge flap deflection as the actuation mechanism and wing-tip displacement as the regulated performance output, incorporating an input-shaping weighting function K_c that governs the trade-off between the degree of structural load alleviation and the associated control effort. Results are obtained for a Global Hawk-like UAV configuration, demonstrating a 23.15% reduction in peak wing-tip deflection under discrete gust excitation and a 10.26% reduction in root-mean-square response under stochastic turbulence; the extensibility of the methodology to a larger, very flexible free-flying-wing platform is also demonstrated. The methodology establishes that $\mathcal{H}_\infty$ controllers designed on low-dimensional ROMs are capable of providing robust gust load alleviation when deployed on the high-dimensional nonlinear aeroelastic system.

Keywords: $\mathcal{H}_\infty$ control, gust load alleviation, flexible aircraft, robust control, reduced-order model

1. Introduction

Active gust load alleviation (GLA) is of paramount importance for ensuring the structural integrity, extending the fatigue life, and improving the ride quality of the emerging class of very flexible aircraft. These platforms, which include high-altitude long-endurance unmanned aerial vehicles (UAVs), solar-powered aircraft, and high-aspect-ratio flying-wing configurations, are characterised by large structural deformations that give rise to pronounced coupling between structural flexibility, unsteady aerodynamic loading, and rigid-body flight dynamics [17,21,22]. In the absence of active control intervention, atmospheric gust encounters can induce substantial wing-tip deflections that lead to excessive structural loads and may trigger aeroelastic instabilities with potentially catastrophic consequences [14]. The structural failure of the NASA Helios prototype during a turbulence encounter [17] provided a stark demonstration of the critical need for effective GLA systems on such platforms, as the combination of large wing deformations and atmospheric disturbances produced a divergent response that the aircraft's conventional autopilot, which lacked any dedicated gust-load-alleviation capability, was unable to arrest.

*Corresponding author. Tel.: +30 210 772 39 30, e-mail: nikolaos.tantaroudas@iccs.gr.
https://doi.org/10.24132/acm.2026.1114

Nomenclature

$\mathbf{B}_c$, $\mathbf{B}_g$	control and gust input matrices	δ	trailing-edge flap deflection
K_c	input-shaping weighting parameter	$\dot{\delta}$	flap angular velocity
m	number of retained ROM modes	$\ddot{\delta}$	flap angular acceleration
n	number of full-order DOF	γ^*	optimal $\mathcal{H}_\infty$ norm
u	control input ($\ddot{\delta}$ in this paper)	λ_k	k-th eigenvalue of the Jacobian
$\mathbf{u}_c$	control input vector	$\mathbf{\Psi}$, $\mathbf{\Phi}$	right, left eigenvector matrices
$\mathbf{u}_d$	gust disturbance vector	DOF	degree of freedom
U_∞	freestream velocity	GLA	gust load alleviation
$\mathbf{w}$	full-order state vector	MAC	mean aerodynamic chord
$\mathbf{w}_{\text{ext}}$	exogenous input vector	NMOR	nonlinear model order reduction
$\mathbf{x}$	augmented state vector	RMS	root mean square
$\mathbf{z}$	reduced-order state vector	ROM	reduced-order model
$\mathbf{z}_{\text{perf}}$	performance output vector	UAV	unmanned aerial vehicle

The fundamental difficulty in designing GLA controllers for very flexible aircraft arises from the intersection of high-dimensional modelling requirements and inherently nonlinear dynamics. Full-order coupled models of the aeroelastic-flight dynamic system typically involve hundreds to thousands of degrees of freedom, a scale at which standard robust control synthesis algorithms become computationally intractable owing to their unfavourable scaling with system dimension. Reduced-order models (ROMs) provide an effective bridge between these competing demands: They compress the essential dynamic behaviour of the coupled system into a compact state-space representation that is amenable to control synthesis, while retaining the key physical coupling mechanisms that govern the gust response [2, 4, 24]. The accuracy of the ROM in representing the input-output behaviour of the full system is therefore a critical prerequisite for the success of the ROM-based control design approach.

The $\mathcal{H}_\infty$ synthesis framework offers a particularly natural formulation for the GLA problem because it explicitly addresses the worst-case disturbance rejection objective: The resulting controller minimises the peak gain from the gust disturbance input to the structural response output, thereby providing guaranteed robustness margins against the modelling uncertainties that inevitably arise from the model reduction process. Prior applications of $\mathcal{H}_\infty$ control to aeroelastic systems have encompassed flutter suppression [5, 20] and manoeuvre load control [3]. The nonlinear dynamic behaviour of aerofoil systems, including the prediction and control of limit-cycle oscillations, has been investigated both experimentally and numerically in [8]. These prior studies have demonstrated the viability of robust control approaches for aeroelastic applications, but a systematic treatment of GLA for geometrically nonlinear flexible aircraft using ROM-based $\mathcal{H}_\infty$ synthesis has been lacking.

In recent years, notable advances have been made in control methodologies for flexible aircraft. Wang et al. [32] developed a nonlinear modal aeroservoelastic framework for flexible aircraft, subsequently extended to nonlinear aeroelastic control using model updating techniques [33]. In [31], Waitman and Marcos demonstrated structured $\mathcal{H}_\infty$ synthesis for active flutter suppression of a flexible-wing UAV demonstrator, confirming the practical applicability of $\mathcal{H}_\infty$ methods to flexible platforms in realistic operating conditions. Artola et al. [1] showed that minimal nonlinear modal descriptions are sufficient for aeroelastic control and estimation through moving-horizon estimation and model-predictive control strategies. A comprehensive treatment of the coupled flight mechanics, aeroelasticity, and control of flexible aircraft is provided in the monograph by Palacios and Cesnik [19], while a detailed case study of $\mathcal{H}_\infty$ and multi-objective control design for a highly flexible blended-wing-body aircraft is presented in the book edited by Kozek and Schirrer [12].

The present paper develops a systematic $\mathcal{H}_\infty$ GLA design framework that builds upon the nonlinear model order reduction (NMOR) methodology introduced in [4, 6] and extended to free-flying aircraft configurations in [25, 26]. The complete aeroservoelastic analysis framework, encompassing the coupling between the structural, aerodynamic, flight dynamic, and control subsystems, is documented in [24]. A self-contained derivation of the NMOR formulation, including third-order Taylor expansion terms and eigenvector selection criteria, is presented in the companion paper [27], while the application of the same ROM framework to rapid worst-case gust identification is demonstrated in [28]. The $\mathcal{H}_\infty$ controller is synthesised on the linearised ROM and subsequently applied to the full nonlinear model to assess its robustness against the unmodelled nonlinearities that are neglected in the design plant. Two test configurations of practical relevance are examined: a Global Hawk-like UAV and a very flexible flying-wing. The role of the input-shaping weighting function in balancing gust alleviation performance against control effort is also discussed.

2. Aeroelastic model and reduction

2.1. Coupled system

The aeroelastic-flight dynamic model integrates three distinct physical subsystems into a unified computational framework. The structural dynamics are represented using geometrically-exact nonlinear beam theory [10, 18], implemented through displacement-based finite elements that carry six degrees of freedom per node, enabling the accurate representation of the arbitrarily large displacements and rotations that characterise very flexible structures. The aerodynamic loading is computed using unsteady strip theory founded on the Theodorsen's thin-aerofoil framework [29], with the Wagner [30] and Küssner [13] indicial functions providing the time-domain unsteady lift build-up due to aerofoil motion and gust penetration, respectively. The aerodynamics is modelled as two-dimensional at each spanwise strip; for the low-velocity, incompressible regime characteristic of large flexible aircraft this representation is sufficient and no three-dimensional or compressibility corrections are applied, with equivalent gust and flight-dynamics studies of such configurations having been reported using the higher-fidelity unsteady vortex-lattice method [15]. The rigid-body flight dynamics are governed by the Newton-Euler equations with quaternion-based attitude propagation [25], which avoids the singularity issues inherent in Euler-angle parametrisations.

The assembled coupled system is expressed in the first-order state-space form as

$$\dot{\mathbf{w}} = \mathbf{R}(\mathbf{w}, \mathbf{u}_c, \mathbf{u}_d), \tag{1}$$

where $\mathbf{w} \in \mathbb{R}^n$ is the state vector, organised into aerodynamic, structural, and rigid-body partitions, $\mathbf{u}_c$ denotes the control input (trailing-edge flap deflection), and $\mathbf{u}_d$ represents the gust disturbance. This formulation captures the full bidirectional coupling between the subsystems, which is essential for the correct prediction of the gust response of very flexible aircraft. The residual $\mathbf{R}$ is nonlinear principally through the geometrically-exact structural kinematics, which retain the arbitrarily large beam displacements and rotations. Although written as a first-order system, equation (1) is the state-space form of an equivalent second-order system in which a configuration-dependent mass matrix multiplies the accelerations and the unsteady aerodynamics contributes additional acceleration-dependent (apparent-mass) loads; these terms are embedded in $\mathbf{R}$ and carried through to the ROM.

Linearisation of this nonlinear system about the trimmed equilibrium state $\mathbf{w}_0$ produces the perturbation equations

$$\dot{\mathbf{w}} = \mathbf{A}\mathbf{w} + \mathbf{B}_c\mathbf{u}_c + \mathbf{B}_g\mathbf{u}_d + \mathbf{F}_{\text{nl}}(\mathbf{w}), \tag{2}$$

where $\mathbf{A}$ is the Jacobian matrix of the coupled system, $\mathbf{B}_c$ and $\mathbf{B}_g$ are the control and gust input matrices, respectively, and $\mathbf{F}_{\text{nl}}$ gathers the higher-order nonlinear terms that are omitted in the linear design plant but retained in the validation model.

2.2. Model order reduction

The NMOR procedure [4, 6, 25] projects the high-dimensional system onto a compact basis of m biorthonormal eigenvectors of the Jacobian: $\Delta\mathbf{w} \approx \mathbf{\Phi}\mathbf{z}$, with $\mathbf{\Psi}^H\mathbf{\Phi} = \mathbf{I}_m$, producing the reduced-order equations for the k-th component of the reduced-order state vector $\mathbf{z}$

$$\dot{z}_k = \lambda_k z_k + \sum_{i,j} D_{kij} z_i z_j + \boldsymbol{\psi}_k^H \mathbf{B}_c \Delta\mathbf{u}_c + \boldsymbol{\psi}_k^H \mathbf{B}_g \Delta\mathbf{u}_d. \tag{3}$$

For the purposes of $\mathcal{H}_\infty$ control design, the linear ROM is employed as the design plant, with the quadratic interaction terms D_{kij} set to zero. The nonlinear terms are retained in the validation model to provide a rigorous assessment of the controller's robustness against the unmodelled nonlinearities that the linear design plant does not capture. This deliberate mismatch between the design plant and the validation model constitutes a stringent test of the controller's robustness properties. The nonlinear equations are advanced in the time-domain using the implicit nonlinear Newmark-β method, in which the nonlinear residual is iterated to convergence at each time step [16].

The UAV test case geometry is depicted in Fig. 1 and the eigenvalue spectrum used for the eigenvector basis selection is presented in Fig. 2. The selection of eigenvalues follows the physically motivated two-tier strategy: Real eigenvalues near the origin capture the rigid-body

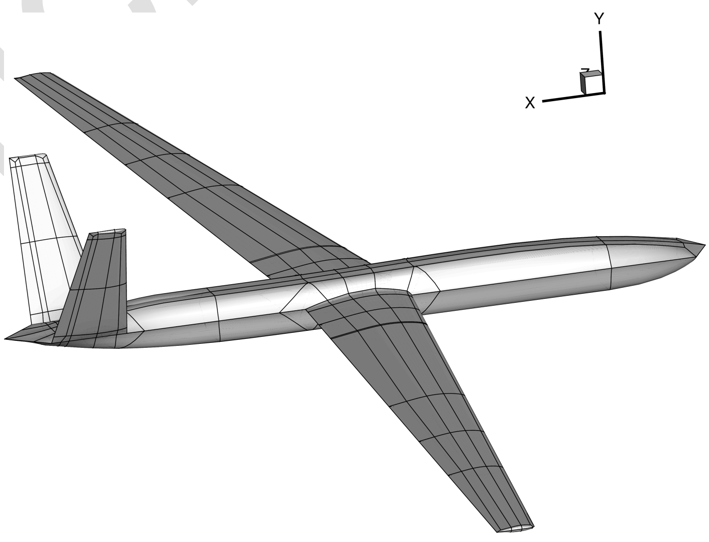

Fig. 1. Surface geometry of the Global Hawk-like UAV; the present aeroelastic model retains the wing as a root-clamped beam, while the fuselage and empennage shown here are not modelled

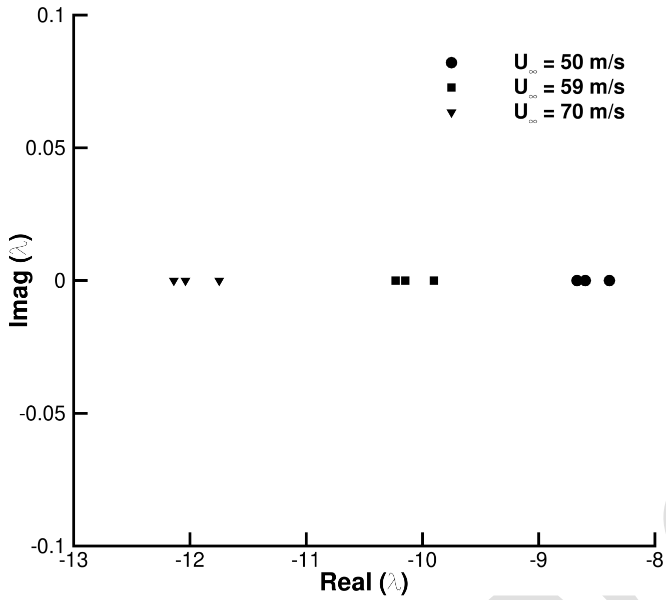

Fig. 2. Variation of the gust mode eigenvalues λ of the coupled Jacobian for the UAV with freestream velocity $U_\infty = \{50,\ 59,\ 70\}$ m/s

and gust coupling dynamics, while lightly damped complex eigenvalues represent the dominant structural bending and torsion modes. These real eigenvalues, referred to here as the *gust-mode eigenvalues*, lie on the real axis because they originate from the indicial (Wagner-Küssner) representation of the unsteady aerodynamics, in which the wake memory is approximated by a small set of first-order exponential lag states [11, 13, 30]. These lag states reproduce the aperiodic build-up and decay of the circulatory lift that follows a change in incidence or a gust encounter; being aerodynamic roots that arise from the unsteady aerodynamics alone, and that are not coupled to the structural inertia, they relax monotonically and therefore possess no oscillatory (imaginary) part. The lightly damped complex-conjugate eigenvalues, by contrast, arise from the second-order elastic dynamics of the flexible structure and consequently retain a finite oscillatory frequency.

While Fig. 2 shows the migration of the real gust-mode eigenvalues with freestream velocity U_∞, the complete set of eigenvalues retained in the UAV reduced-order basis is listed in Table 1: five lightly damped complex structural modes (the first to fourth bending modes and the first torsion mode), together with three real gust modes.

3. $\mathcal{H}_\infty$ control design

3.1. Control architecture

The GLA control architecture is depicted schematically in Fig. 3. The measurement output available to the controller is the wing-root bending moment M, which is adopted here as the feedback signal because it constitutes the standard scalar measurement for gust load alleviation: It is directly representative of the structural load that the controller seeks to alleviate, and it is physically realisable with a single sensor—in practice a strain-gauge bridge installed at the wing root—without requiring distributed sensing along the span. For the configurations considered in this work, whose gust response is dominated by the first bending mode, the wing-root bending moment is monotonically related to the wing-tip displacement, so that the two quantities may be

Table 1. Real and imaginary parts of eigenvalues retained in the eight-mode UAV reduced-order basis at $U_\infty = 59$ m/s

Mode	Mode shape	Real part [Hz]	Imaginary part [Hz]
1	First bending	–0.882	1.97
2	Second bending	–0.804	9.81
3	First torsion	–0.171	14.5
4	Third bending	–0.703	21.7
5	Fourth bending	–0.604	41.9
6	Gust mode	–9.90	0
7	Gust mode	–1.01	0
8	Gust mode	–1.02	0

used interchangeably as the scalar feedback measurement. The control input is the trailing-edge flap angular acceleration $\ddot{\delta}$. The trailing-edge flap is distributed over the full span, each beam element carrying its own control surface whose unsteady aerodynamic effect is represented through the Theodorsen control-surface terms [29]; all surfaces deflect in unison, so that the single scalar command δ denotes the common flap deflection applied across the wing. The flap dynamics are represented by a second-order kinematic (double-integrator) actuator model

$$\dot{\mathbf{x}}_{\text{act}} = \begin{bmatrix} 0 & 1 \\ 0 & 0 \end{bmatrix} \mathbf{x}_{\text{act}} + \begin{bmatrix} 0 \\ 1 \end{bmatrix} u, \qquad \mathbf{x}_{\text{act}} = \begin{bmatrix} \delta \\ \dot{\delta} \end{bmatrix}, \tag{4}$$

where $u = \ddot{\delta}$ is the commanded flap angular acceleration. No physical servo is modelled: The flap enters the aeroelastic system solely through its unsteady aerodynamic effect, represented by the Theodorsen control-surface terms [29]. The double integrator is therefore a purely kinematic command-shaping device that, by taking the commanded acceleration as the design input, guarantees that the flap deflection and its rate evolve continuously and yields smooth, physically realisable command histories without prescribing an arbitrary servo natural frequency or damping ratio. The control-effort penalty $K_c u$ acts directly on the commanded acceleration and,

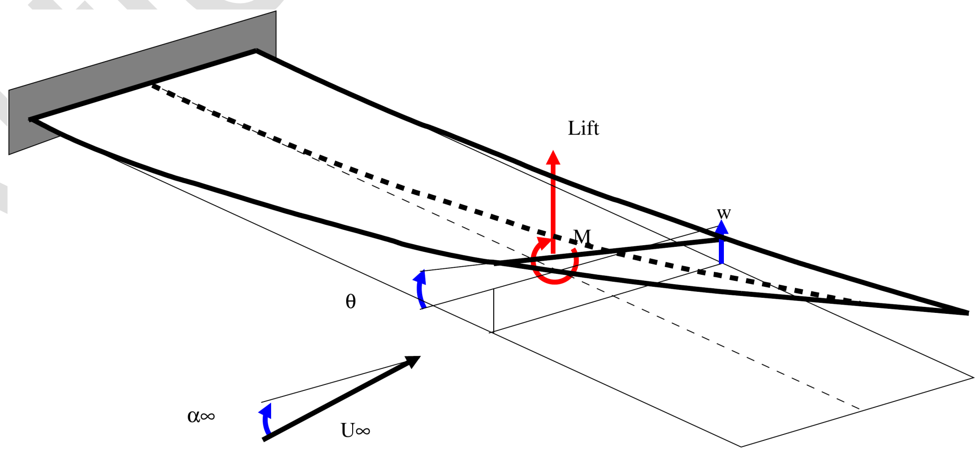

Fig. 3. Wing deformation under gust loading showing the open-loop (*dashed*) and closed-loop (*solid*) responses; α_∞ is the angle of attack of the free-stream velocity U_∞ and θ is the torsional (twist) rotation of the wing section

through the integrator chain, bounds the resulting flap rate and deflection.

3.2. Augmented plant

The linear ROM is augmented with the actuator dynamics to construct the design plant for $\mathcal{H}_\infty$ synthesis

$$\dot{\mathbf{x}} = \mathbf{A}_p\mathbf{x} + \mathbf{B}_w\mathbf{w}_{\text{ext}} + \mathbf{B}_u u, \tag{5}$$

where $\mathbf{x} = \{\mathbf{z}, \delta, \dot{\delta}\}^T$ is the augmented state vector that encompasses both the aeroelastic ROM states and the actuator states, $\mathbf{w}_{\text{ext}}$ is the exogenous input representing the gust disturbance, and the system matrices take the following form:

$$\mathbf{A}_p = \begin{bmatrix} \mathbf{\Lambda} & \mathbf{\Psi}^H\mathbf{B}_c\mathbf{e}_\delta & \mathbf{0} \\ \mathbf{0} & 0 & 1 \\ \mathbf{0} & 0 & 0 \end{bmatrix}, \quad \mathbf{B}_w = \begin{bmatrix} \mathbf{\Psi}^H\mathbf{B}_g \\ 0 \\ 0 \end{bmatrix}, \quad \mathbf{B}_u = \begin{bmatrix} \mathbf{0} \\ 0 \\ 1 \end{bmatrix}, \tag{6}$$

where $\mathbf{\Lambda} = \operatorname{diag}(\lambda_1, \ldots, \lambda_m)$ is the diagonal matrix containing the retained eigenvalues and $\mathbf{e}_\delta$ is the mapping vector that connects the flap angle to the aerodynamic input channel of the ROM.

3.3. $\mathcal{H}_\infty$ problem formulation

The generalised plant is assembled following the standard two-port framework for robust control synthesis

$$\begin{bmatrix} \mathbf{z}_{\text{perf}} \\ \mathbf{y}_{\text{meas}} \end{bmatrix} = \begin{bmatrix} \mathbf{P}_{11} & \mathbf{P}_{12} \\ \mathbf{P}_{21} & \mathbf{P}_{22} \end{bmatrix} \begin{bmatrix} \mathbf{w}_{\text{ext}} \\ u \end{bmatrix}, \tag{7}$$

where $\mathbf{z}_{\text{perf}}$ is the performance output vector that the controller seeks to minimise, $\mathbf{y}_{\text{meas}}$ is the measured output vector that is available to the controller for feedback, and $\mathbf{P}_{11}$, $\mathbf{P}_{12}$, $\mathbf{P}_{21}$, $\mathbf{P}_{22}$ are the four sub-blocks of the generalised plant transfer-function matrix $\mathbf{P}$ with the first subscript referring to the output (1: $\mathbf{z}_{\text{perf}}$, 2: $\mathbf{y}_{\text{meas}}$) and the second one to the input (1: $\mathbf{w}_{\text{ext}}$, 2: u).

An input-shaping weighting function characterised by the scalar parameter K_c is introduced to penalise the magnitude of the control effort as

$$\mathbf{z}_{\text{perf}} = \begin{bmatrix} \mathbf{C}_z\mathbf{x} \\ K_c u \end{bmatrix}, \tag{8}$$

where $\mathbf{C}_z$ is the output matrix that selects the regulated quantity, namely the wing-tip displacement. The $\mathcal{H}_\infty$ optimisation then seeks a stabilising controller $K(s)$ that minimises the closed-loop $\mathcal{H}_\infty$ norm

$$\gamma^* = \min_{K \text{ stabilising}} \|\mathcal{F}_l(\mathbf{P}, K)\|_\infty = \min_K \sup_\omega \bar{\sigma}\left[\mathcal{F}_l(\mathbf{P}, K)(j\omega)\right], \tag{9}$$

where ω is the angular frequency, j is the imaginary unit, $\mathcal{F}_l$ denotes the lower linear fractional transformation that maps the exogenous input to the performance output through the closed-loop interconnection, and $\bar{\sigma}$ is the maximum singular value. The optimal value γ^* represents the minimum achievable worst-case amplification from the gust disturbance to the performance output. The controller is obtained as the optimal $\mathcal{H}_\infty$ solution of this problem by means of the Riccati-based algorithm of Doyle et al. [7], as implemented in the `hinfsyn` routine of the MATLAB Robust Control Toolbox; the synthesis performs the γ-iteration that recovers the minimal γ^* together with the associated stabilising controller [23, 35].

3.4. Role of the weighting parameter K_c

The weighting parameter K_c plays a central role in shaping the controller behaviour by governing the penalty applied to the control effort. Larger values of K_c impose a more stringent penalty on the flap deflection, producing controllers that command smaller actuator motions at the expense of reduced gust alleviation effectiveness. Conversely, smaller values of K_c permit more aggressive control action, achieving greater load reduction but with potentially larger flap deflections that may approach actuator saturation limits. The value $K_c = 1$ adopted throughout this paper is the weighting previously identified as giving the most favourable load-alleviation/control-effort compromise for this class of problem in the parametric study of [24]. Rather than repeating that optimisation, the present work adopts this established value and concentrates on a distinct question: Whether a controller synthesised on the low-order ROM retains its performance and robustness when deployed on the high-dimensional nonlinear model. It should be emphasised, however, that the effect of K_c on the achieved load-alleviation/control-effort compromise is case-dependent: The optimal weighting varies with the aircraft configuration, the structural flexibility, the available actuator authority and the gust environment, so the value identified in [24] cannot be assumed to be universally optimal. The adoption of the single design point $K_c = 1$ therefore constitutes a limitation of the present study, and a configuration-specific retuning of K_c would be required in a detailed design application.

4. Results

4.1. Global Hawk-like UAV

The UAV configuration features a 17.75-meter semi-span wing discretised using 20 beam elements, yielding a full-order model with $n = 540$ degrees of freedom (DOFs) that is reduced to an $m = 8$ mode ROM [24,26]. The wing is modelled as a root-clamped cantilever: The fuselage and empennage are not represented and the root is fully restrained, so this configuration contains no rigid-body DOFs and the controller acts solely on the elastic gust response. Consistently, the eight retained modes comprise five lightly damped structural modes (first to fourth bending and first torsion) and three real gust modes, with no rigid-body modes, see Table 1. The three-view geometry of the aircraft is shown in Fig. 4. The operating conditions are: freestream velocity $U_\infty = 59$ m/s, air density $\varrho = 0.0789$ kg/m^3 corresponding to high altitude, and trim angle of attack $\alpha_0 = 4^\circ$. The static aeroelastic deformation of the wing at this condition is illustrated in Fig. 5.

The first two wing bending modes, being the lowest-frequency flexible modes, are the most strongly excited by the predominantly low-frequency content of the gust and are therefore the primary targets of the GLA controller; their mode shapes are depicted in Fig. 6.

4.1.1. Discrete gust response

The worst-case "1-minus-cosine" discrete gust for this configuration has a duration of approximately 4 s (corresponding to 197 MAC) and a peak velocity equal to 14 % of the freestream velocity. Fig. 7 presents the closed-loop wing-tip displacement and trailing-edge flap deflection time histories, compared against the open-loop (uncontrolled) response.

The controller responds to the gust encounter by commanding an initial downward flap rotation, which generates a nose-down pitching moment that partially counteracts the lift increment induced by the gust. The temporal profile of the flap deflection exhibits a smooth bell-shaped characteristic, which is consistent with the double-integrator actuator model specified in (4) and

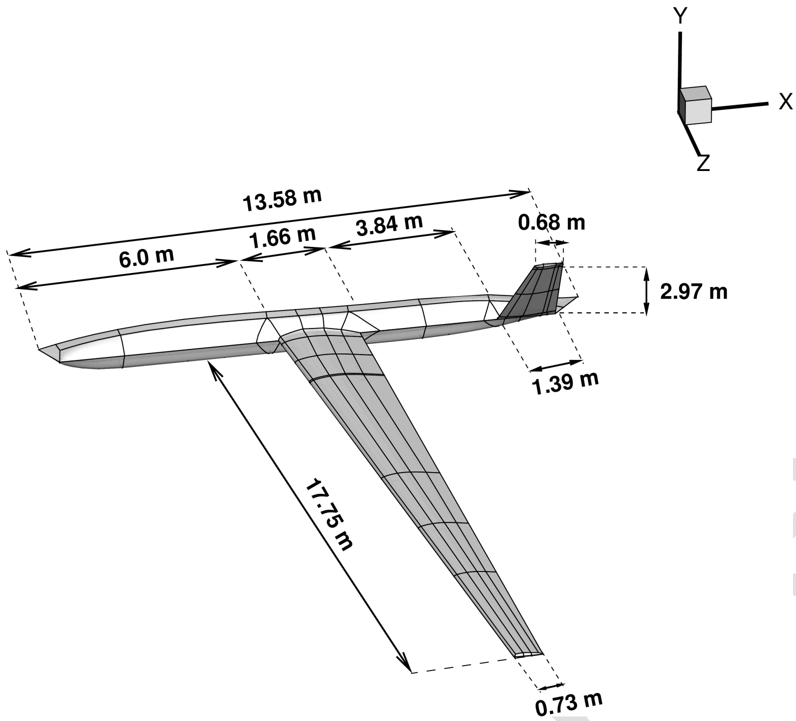

Fig. 4. Three-view geometry of the Global Hawk-like UAV showing the wing, fuselage, horizontal stabiliser, and vertical tail

ensures that the commanded motion is physically realisable. The closed-loop wing-tip response demonstrates both a significant reduction in peak amplitude and an enhanced rate of damping during the post-gust oscillatory decay, indicating that the controller provides beneficial effects both during and after the gust encounter. These metrics are quantified in Table 2, which reports a 23.15% reduction in peak wing-tip deflection at a maximum flap rotation of 9.47°.

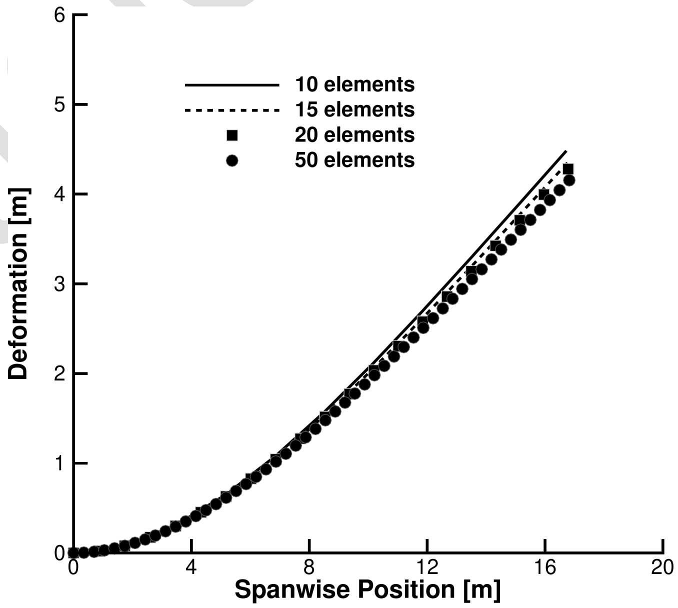

Fig. 5. Mesh convergence of the static aeroelastic wing deformation of the UAV at the static aeroelastic equilibrium ($U_\infty = 59$ m/s, $\alpha_0 = 4°$) for 10, 15, 20, and 50 beam elements

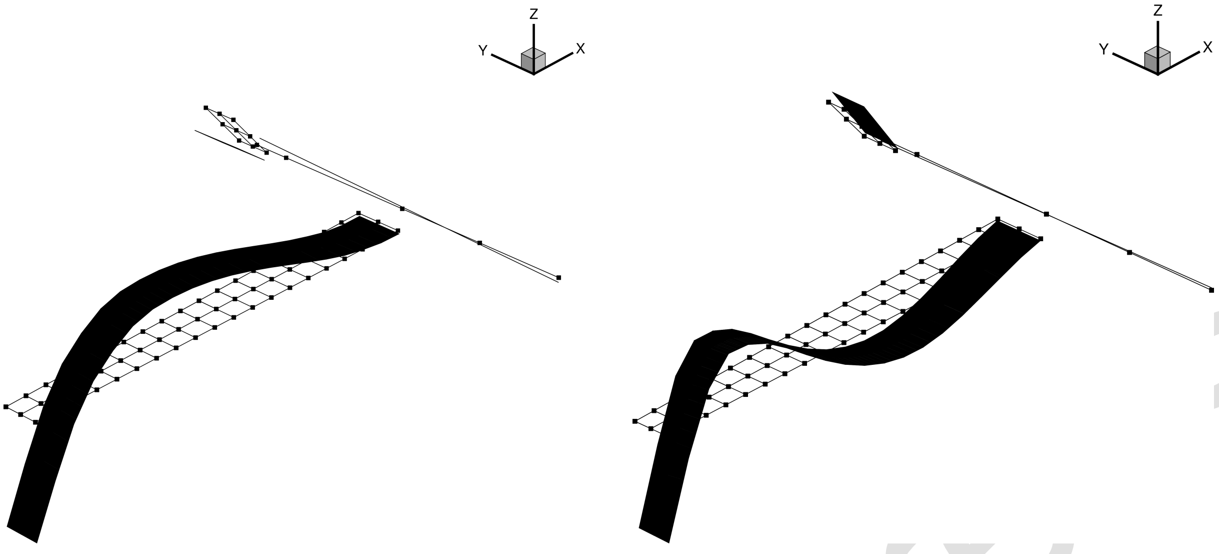

Fig. 6. Structural mode shapes of the UAV wing: (a) first wing bending mode and (b) second wing bending mode

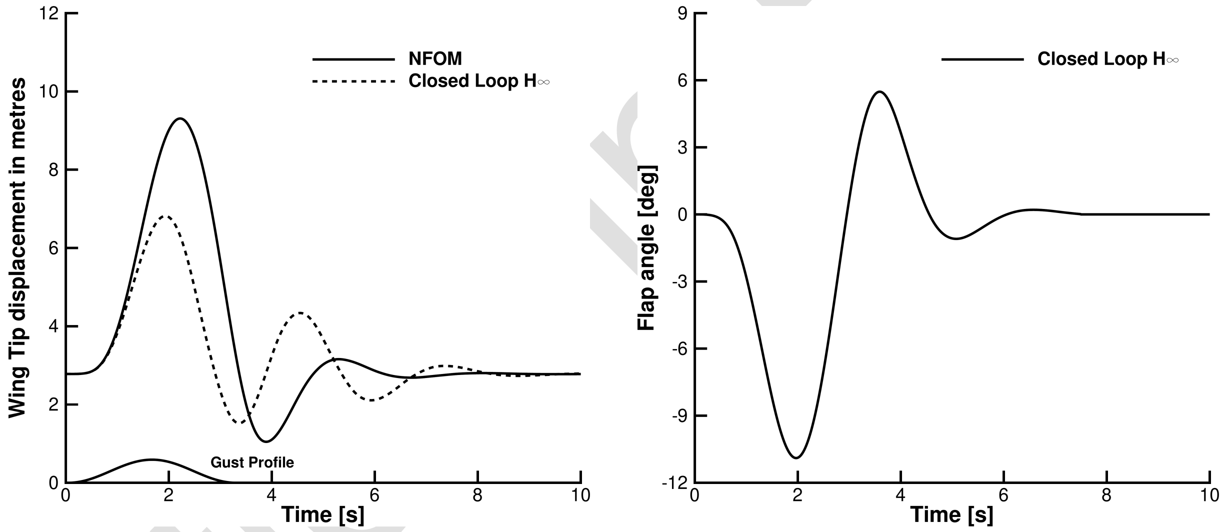

Fig. 7. $\mathcal{H}_\infty$ GLA performance under worst-case discrete gust (UAV, $K_c = 1$): (a) wing-tip vertical displacement and (b) trailing-edge flap deflection. Open loop (*solid*) and closed loop (*dashed*)

Table 2. $\mathcal{H}_\infty$ GLA performance metrics under discrete gust (UAV, $K_c = 1$)

Metric	Open loop	Closed loop ($K_c = 1$)
Wing-tip deflection reduction	—	–23.15 %
Max flap rotation	—	–9.47°

4.1.2. Stochastic turbulence response

The closed-loop performance under von Kármán continuous turbulence (with turbulence scale length $L_w = 750\,\text{m}$) is presented in Fig. 8. This test case provides a more stringent assessment

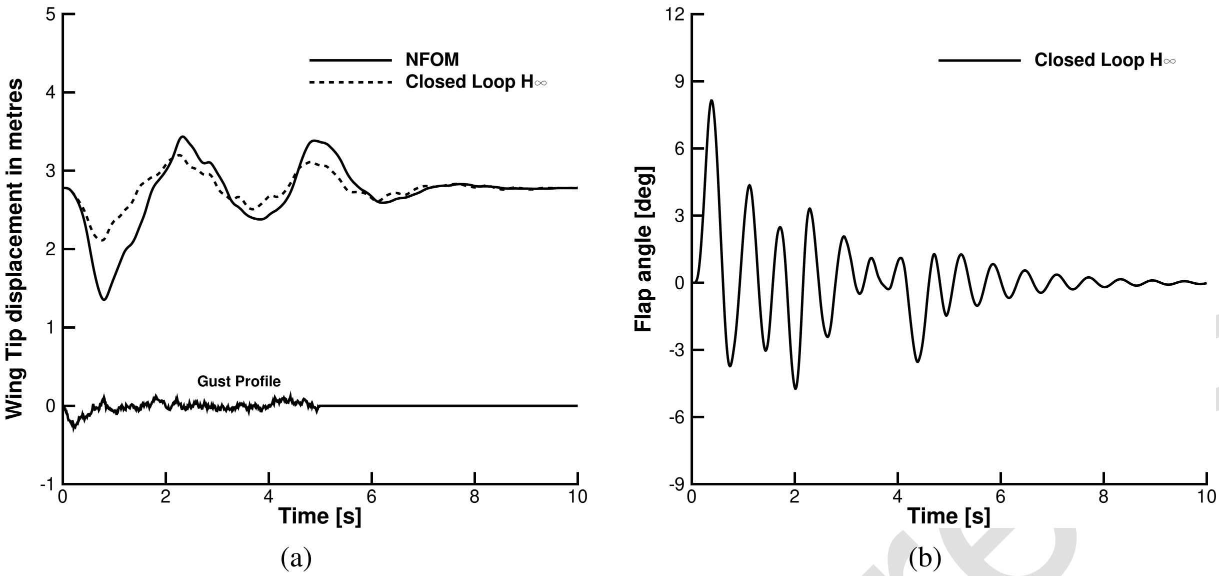

Fig. 8. $\mathcal{H}_\infty$ GLA performance under von Kármán stochastic turbulence (UAV, $K_c = 1$): (a) wing-tip vertical displacement and (b) trailing-edge flap deflection. Open loop (*solid*) and closed loop (*dashed*)

of the controller than the discrete gust, as the turbulence contains energy distributed across a broad frequency spectrum.

These turbulence metrics are summarised in Table 3. It should be noted that the discrete-gust and turbulence results measure different quantities—a peak-amplitude reduction for the deterministic discrete gust and a root-mean-square (RMS) reduction for the stochastic turbulence—and are therefore not directly comparable, each being the natural metric for its disturbance type. The smaller RMS reduction under stochastic turbulence (10.26 %) relative to the peak reduction under the discrete gust (23.15 %) can be attributed to the broadband nature of the von Kármán frequency spectrum. The $\mathcal{H}_\infty$ controller effectively attenuates the disturbance energy that falls within its design bandwidth, which is determined by the frequency range of the modes retained in the eight-mode ROM. However, the higher-frequency turbulence components that excite structural modes beyond the ROM bandwidth are less effectively attenuated by the controller [6]. This interpretation is offered as a plausible explanation rather than a demonstrated one; confirming it would require a dedicated sensitivity study with progressively larger ROM bases. Subject to that caveat, improved continuous-turbulence rejection may be achievable through either a larger ROM basis capturing additional high-frequency modes or a complementary adaptive control strategy.

4.2. Model convergence and extension

Fig. 9a presents the mesh convergence of the static aeroelastic solution for the very flexible flying-wing configuration (32-meter span, 16-meter semi-span, $n = 1\,616$ DOF, $m = 9$ ROM

Table 3. $\mathcal{H}_\infty$ GLA performance under von Kármán turbulence (UAV, $K_c = 1$)

Metric	Open loop	Closed loop ($K_c = 1$)
RMS wing-tip deflection	baseline	–10.26 %
Max flap rotation	—	±12.79°

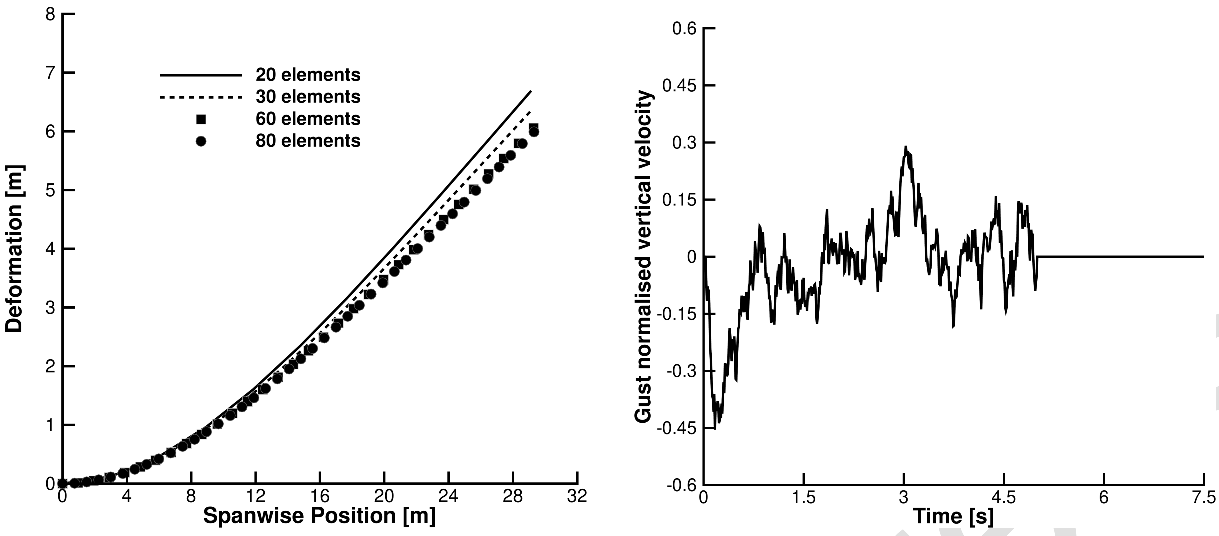

(a) (b)

Fig. 9. (a) Mesh convergence of the nonlinear static wing deformation for the very flexible flying-wing (32-meter span) with increasing number of beam elements, and (b) sample von Kármán turbulence velocity profile

modes), demonstrating that 80 beam elements adequately resolve the nonlinear wing deformation for this larger platform. In contrast to the cantilever UAV, the flying-wing is treated as a free-flying configuration in which the rigid-body degrees of freedom are retained [25], so that its nine-mode basis comprises four real eigenvalues (associated with the rigid-body and gust coupling) and five lightly damped complex pairs. This study verifies that the static aeroelastic solution is spatially converged for this larger and more flexible configuration; it does not by itself establish the dynamic applicability of the approach, which rests instead on the reduced-order modelling validated against the nonlinear full-order model. A representative von Kármán turbulence velocity profile employed in the stochastic gust simulations is shown in Fig. 9b.

5. Discussion

The results presented above give rise to several observations regarding the performance and applicability of the $\mathcal{H}_\infty$ GLA framework that merit further discussion.

The robustness of the ROM-based controller design is perhaps the most practically significant finding. The $\mathcal{H}_\infty$ controller, synthesised on the eight-mode linear ROM, delivers consistent and effective load alleviation when applied to the 540-DOF nonlinear full-order model, despite the substantial model reduction and the deliberate omission of nonlinear terms in the design plant. This robustness can be attributed to the inherent conservatism embedded within the $\mathcal{H}_\infty$ synthesis framework, which accounts for worst-case disturbance amplification across all frequencies and thereby provides implicit robustness against the unmodelled nonlinearities that are present in the full-order system but absent from the design plant.

The asymmetry between the discrete gust and stochastic turbulence performance warrants careful interpretation. The controller achieves a 23.15% reduction in peak response under discrete gusts and a 10.26% reduction in RMS response under stochastic turbulence; although these are distinct metrics and therefore not directly comparable, the difference has a clear physical explanation rooted in the frequency-domain characteristics of the two disturbance types. Although the “1-minus-cosine” gust is a transient disturbance with a broadband spectrum, the bulk of its energy is concentrated in a narrow band about the characteristic frequency $f_g = U_\infty/(2H_g)$ associated with its $2H_g$ spatial wavelength [9], and for the cases considered, this band falls within the controller bandwidth, enabling effective targeted attenuation. Stochastic turbulence, by contrast, distributes its energy across a broad frequency spectrum and the controller can only attenuate the portion of this energy that lies within its bandwidth, which is fundamentally limited by the frequency range of the retained modes. For applications where stochastic turbulence rejection is of primary importance, adaptive controllers that can adjust their response characteristics in real time to track the evolving turbulence spectrum may offer superior performance [26].

Regarding practical actuator constraints, the maximum flap rotation of approximately 10° at $K_c = 1$ falls within the typical authority range of trailing-edge control surfaces on UAV platforms. However, the current modelling framework does not incorporate explicit actuator rate and magnitude saturation limits, nor does it account for hinge moment constraints that may limit the available control authority in practice. In a detailed design implementation, these constraints would be addressed through the inclusion of additional weighting functions in the generalised plant or through the adoption of a mixed $\mathcal{H}_2/\mathcal{H}_\infty$ formulation that can accommodate hard constraints on the control signal.

A further consideration concerns the suppression of the first peak in the wing-root bending moment, which a purely feedback architecture can only partially attenuate, since the controller must first sense the gust-induced response before acting. In practice, the first-peak load is most effectively reduced by feedforward control driven by an upstream gust measurement—for example, from a nose-mounted flow vane or LiDAR (Light Detection And Ranging)—as demonstrated for large flexible transport aircraft by Wildschek [34]. Augmenting the present $\mathcal{H}_\infty$ feedback design with such a feedforward channel is therefore a natural extension of this work.

The same GLA methodology has been extended to the 32-meter span very flexible flying-wing configuration ($n = 1\,616$ DOF, $m = 9$ ROM modes) in [25], where the controller successfully reduced wing-tip deflections while maintaining the desired trim flight condition. The mesh convergence for this configuration is illustrated in Fig. 9a. The significantly larger structural deformations characteristic of this configuration introduce stronger nonlinear effects; while the intrinsic robustness margin of the $\mathcal{H}_\infty$ design is expected to accommodate these nonlinearities, a full quantitative GLA assessment for the flying-wing was not repeated here and is left to future work.

6. Conclusions

An $\mathcal{H}_\infty$ robust control framework for gust load alleviation of very flexible aircraft exhibiting geometrically nonlinear structural behaviour has been presented and validated. The controller is synthesised on a compact reduced-order model and assessed against the full nonlinear system to verify its robustness. The eight-mode ROM-based $\mathcal{H}_\infty$ controller achieves a 23.15% reduction in peak wing-tip deflection under worst-case discrete gust excitation and a 10.26% reduction in RMS response under stochastic von Kármán turbulence, when applied to the 540-DOF nonlinear full-order model. The input-shaping weighting parameter K_c provides a systematic single-parameter mechanism for adjusting the trade-off between structural load alleviation and control effort; the value $K_c = 1$, previously identified in [24] as the most favourable compromise for this class of problem, is adopted throughout, noting that its effect is case-dependent and that a retuning would be required for other configurations or gust environments. Superior alleviation performance is obtained for longer-duration discrete gusts whose dominant frequency content falls within the controller design bandwidth, which is consistent with the frequency-domain interpretation of $\mathcal{H}_\infty$ optimality. The framework has been demonstrated to be directly extensible to larger and more flexible configurations, including the 1 616-DOF flying-wing, as well as to models employing higher-fidelity aerodynamic representations [2, 24]. For applications requiring enhanced stochastic turbulence attenuation, adaptive control strategies offer a promising complementary approach to the $\mathcal{H}_\infty$ design [26].

Acknowledgements

This work was supported by the U.K. Engineering and Physical Sciences Research Council (EPSRC) grant EP/I014594/1 on "Nonlinear Flexibility Effects on Flight Dynamics and Control of Next-Generation Aircraft." The authors are grateful to Prof. A. Da Ronch and Prof. K. J. Badcock for their valuable guidance on flight dynamics modelling.

References

[1] Artola, M., Goizueta, N., Wynn, A., Palacios, R., Aeroelastic control and estimation with a minimal nonlinear modal description, AIAA Journal 59 (7) (2021) 2 697–2 713. https://doi.org/10.2514/1.J060018

[2] Da Ronch, A., Badcock, K., Wang, Y., Wynn, A., Palacios, R., Nonlinear model reduction for flexible aircraft control design, Proceedings of the AIAA Atmospheric Flight Mechanics Conference, AIAA Paper 2012-4404, Minneapolis, 2012, pp. 1–23. https://doi.org/10.2514/6.2012-4404

[3] Da Ronch, A., McCracken, A. J., Tantaroudas, N. D., Badcock, K. J., Hesse, H., Palacios, R., Assessing the impact of aerodynamic modelling on manoeuvring aircraft, Proceedings of the AIAA Atmospheric Flight Mechanics Conference (AIAA SciTech 2014), AIAA Paper 2014-0732, National Harbor, 2014, pp. 1–16. https://doi.org/10.2514/6.2014-0732

[4] Da Ronch, A., Tantaroudas, N. D., Badcock, K. J., Reduction of nonlinear models for control applications, Proceedings of the 54th AIAA/ASME/ASCE/AHS/ASC Structures, Structural Dynamics, and Materials Conference, AIAA Paper 2013-1491, Boston, 2013, pp. 1–19. https://doi.org/10.2514/6.2013-1491

[5] Da Ronch, A., Tantaroudas, N. D., Jiffri, S., Mottershead, J. E., A nonlinear controller for flutter suppression: From simulation to wind tunnel testing, Proceedings of the 55th AIAA/ASME/ASCE/AHS/SC Structures, Structural Dynamics, and Materials Conference, AIAA Paper 2014-0345, National Harbor, 2014, pp. 1–19. https://doi.org/10.2514/6.2014-0345

[6] Da Ronch, A., Tantaroudas, N. D., Timme, S., Badcock, K. J., Model reduction for linear and nonlinear gust loads analysis, Proceedings of the 54th AIAA/ASME/ASCE/AHS/ASC Structures, Structural Dynamics, and Materials Conference, AIAA Paper 2013-1492, Boston, 2013, pp. 1–18. https://doi.org/10.2514/6.2013-1492

[7] Doyle, J. C., Glover, K., Khargonekar, P. P., Francis, B. A., State-space solutions to standard $\mathcal{H}_2$ and $\mathcal{H}_\infty$ control problems, IEEE Transactions on Automatic Control 34 (8) (1989) 831–847. https://doi.org/10.1109/9.29425

[8] Fichera, S., Jiffri, S., Wei, X., Da Ronch, A., Tantaroudas, N., Mottershead, J. E., Experimental and numerical study of nonlinear dynamic behaviour of an aerofoil, Proceedings of the ISMA 2014 Conference on Noise and Vibration Engineering, 2014, pp. 3 609–3 618.

[9] Hoblit, F. M., Gust loads on aircraft: Concepts and applications, AIAA Education Series, Washington, American Institute of Aeronautics and Astronautics (AIAA), 1988. https://doi.org/10.2514/4.861888

[10] Hodges, D. H., Geometrically exact, intrinsic theory for dynamics of curved and twisted anisotropic beams, AIAA Journal 41 (6) (2003) 1 131–1 137. https://doi.org/10.2514/2.2054

[11] Jones, R. T., Operational treatment of the non-uniform lift theory in airplane dynamics, NACA Technical Report TN-667, NASA, 1938.

[12] Kozek, M., Schirrer, A., Modeling and control for a blended wing body aircraft: A case study, Cham, Springer, 2015. https://doi.org/10.1007/978-3-319-10792-9

[13] Küssner, H., Summary report on the unsteady lift of wings, Luftfahrtforschung 13 (12) (1936) 410–424. (in German)

[14] Livne, E., Aircraft active flutter suppression: State of the art and technology maturation needs, Journal of Aircraft 55 (1) (2018) 410–452. https://doi.org/10.2514/1.C034442

[15] Murua, J., Palacios, R., Graham, J. M. R., Applications of the unsteady vortex-lattice method in aircraft aeroelasticity and flight dynamics, Progress in Aerospace Sciences 55 (2012) 46–72. https://doi.org/10.1016/j.paerosci.2012.06.001

[16] Newmark, N. M., A method of computation for structural dynamics, Journal of the Engineering Mechanics Division 85 (3) (1959) 67–94. https://doi.org/10.1061/JMCEA3.0000098

[17] Noll, T. E., Brown, J. M., Perez-Davis, M. E., Ishmael, S. D., Tiffany, G. C., Gaier, M., Investigation of the Helios prototype aircraft mishap, NASA Report, 2004.

[18] Palacios, R., Nonlinear normal modes in an intrinsic theory of anisotropic beams, Journal of Sound and Vibration 330 (8) (2011) 1 772–1 792. https://doi.org/10.1016/j.jsv.2010.10.023

[19] Palacios, R., Cesnik, C., Dynamics of flexible aircraft: Coupled flight mechanics, aeroelasticity, and control, Cambridge Aerospace Series Vol. 25, Cambridge University Press, 2023. https://doi.org/10.1017/9781108354868

[20] Papatheou, E., Tantaroudas, N., Da Ronch, A., Cooper, J., Mottershead, J., Active control for flutter suppression: An experimental investigation, Proceedings of the International Forum on Aeroelasticity and Structural Dynamics, IFASD Paper 2013-8D, 2013, pp. 1–14.

[21] Patil, M. J., Hodges, D. H., Flight dynamics of highly flexible flying wings, Journal of Aircraft 43 (6) (2006) 1 790–1 799. https://doi.org/10.2514/1.17640

[22] Patil, M. J., Hodges, D. H., Cesnik, C. E. S., Nonlinear aeroelasticity and flight dynamics of high-altitude long-endurance aircraft, Journal of Aircraft 38 (1) (2001) 88–94. https://doi.org/10.2514/2.2738

[23] Skogestad, S., Postlethwaite, I., Multivariable feedback control: Analysis and design, 2nd edition, Chichester, John Wiley & Sons, 2005.

[24] Tantaroudas, N. D., Da Ronch, A., Nonlinear reduced-order aeroservoelastic analysis of very flexible aircraft, In: Advanced UAV aerodynamics, flight stability and control: Novel concepts, theory and applications, Chichester, John Wiley & Sons, 2017, pp. 143–179. https://doi.org/10.1002/9781118928691.ch4

[25] Tantaroudas, N. D., Da Ronch, A., Badcock, K. J., Palacios, R., Model order reduction for control design of flexible free-flying aircraft, Proceedings of the AIAA Atmospheric Flight Mechanics Conference (AIAA SciTech 2015), AIAA Paper 2015-0240, Kissimmee, 2015, pp. 1–24. https://doi.org/10.2514/6.2015-0240

[26] Tantaroudas, N. D., Da Ronch, A., Gai, G., Badcock, K. J., Palacios, R., An adaptive aeroelastic control approach using nonlinear reduced order models, Proceedings of the 14th AIAA Aviation Technology, Integration, and Operations Conference, AIAA Paper 2014-2590, Atlanta, 2014, pp. 1–21. https://doi.org/10.2514/6.2014-2590

[27] Tantaroudas, N. D., Karachalios, I., Nonlinear model order reduction for coupled aeroelastic-flight dynamic systems, arXiv:2603.15296 (2026) 1–23. (preprint) https://doi.org/10.48550/arXiv.2603.15296

[28] Tantaroudas, N. D., Karachalios, I., Rapid worst-case gust identification for very flexible aircraft using reduced-order models, arXiv:2603.16212 (2026) 1–14. (preprint) https://doi.org/10.48550/arXiv.2603.16212

[29] Theodorsen, T., General theory of aerodynamic instability and the mechanism of flutter, Report NACA-TR-496, NASA, 1935.

[30] Wagner, H., On the generation of dynamic lift by airfoils, Zeitschrift für Angewandte Mathematik und Mechanik 5 (1) (1925) 17–35. (in German) https://doi.org/10.1002/zamm.19250050103

[31] Waitman, S., Marcos, A., $\mathcal{H}_\infty$ control design for active flutter suppression of flexible-wing unmanned aerial vehicle demonstrator, Journal of Guidance, Control, and Dynamics 43 (4) (2020) 656–672. https://doi.org/10.2514/1.G004618

[32] Wang, Y., Wynn, A., Palacios, R., Nonlinear modal aeroservoelastic analysis framework for flexible aircraft, AIAA Journal 54 (10) (2016) 3 075–3 090. https://doi.org/10.2514/1.J054537

[33] Wang, Y., Wynn, A., Palacios, R., Nonlinear aeroelastic control of very flexible aircraft using model updating, Journal of Aircraft 55 (4) (2018) 1 551–1 563. https://doi.org/10.2514/1.C034684

[34] Wildschek, A., An adaptive feed-forward controller for active wing bending vibration alleviation on large transport aircraft, Ph.D. thesis, Technical University of Munich, Munich, 2009.

[35] Zhou, K., Doyle, J. C., Glover, K., Robust and optimal control, Upper Saddle River, Prentice Hall, 1996.